

Some Statistical Aspects of Ice-Crystal Orientation Fabrics

M. Hay¹, E.D. Waddington¹

¹*Department of Earth and Space Sciences, University of Washington*

ABSTRACT. Ice crystal c-axis orientation fabric has a large effect on polycrystalline ice flow due to the strong plastic anisotropy of individual grains. The crystal c-axis orientation fabric can be described as an orientation distribution function (ODF), which is a probability distribution defined on the sphere for the direction of crystal c-axes. From this viewpoint, we present several statistical results for ODFs. We introduce a parameterized ODF (PODF), the Bingham distribution, to glaciology. We compare the performance of this and other PODFs against measurements from the West Antarctic Ice Sheet (WAIS) and Siple Dome ice cores. We also examine the sampling error introduced by attempting to infer the underlying ODF from a limited thin-section sample. We introduce new analytical expressions for sampling error, and examine the use of bootstrapping for estimation of sampling error. We show that sampling error of an estimate of the enhancement factor in simple shear can be large.

INTRODUCTION

An individual ice crystal has an anisotropic creep response, deforming most easily in shear parallel to the crystal basal-plane, orthogonal to the crystallographic c-axis. Plastic deformation of an ice polycrystal depends on the orientations of its constituent grains (e.g. Azuma 1994), which is described by the c-axis orientation distribution function (ODF). The ODF is a probability distribution of c-axis orientation density often defined on the upper hemisphere (because a c-axis vector \mathbf{c} is indistinguishable from $-\mathbf{c}$). In this paper, we will instead treat the ODF as being an even function defined on the entire sphere for mathematical convenience. A polycrystal with an isotropic ODF will have a bulk isotropic response to applied stress. However, ice polycrystals develop an anisotropic ODF in response to applied strain (Azuma and Higashi 1985, Alley 1992). The development of a preferred orientation is guided primarily by basal slip. This causes a tendency for the c-axes to rotate away from the directions of principal extensional strain (Azuma and Goto-Azuma, 1996). Other processes also affect c-axis fabric development. Highly strained grains may polygonize, where subgrains increasingly rotate with respect to one

Table 1. List of symbols

Symbol	Definition
q_i	Component of a tensor in index notation
\mathbf{q}	Same tensor in vector notation
\hat{x}	A random variable
\tilde{x}	A realization of \hat{x} upon measurement
c_i	ice-crystal c-axis for $i = 1, 2, 3$ in x, y, z directions
$\psi(\mathbf{c})$	Ice-crystal orientation dist. func.
$\langle \hat{x} \rangle$	Expected value of \hat{x} under ψ
a_{ij}	Grain structure-tensor $c_i c_j$
A_{ij}	Comp. of the 2 th order orient. tensor $\langle a_{ij} \rangle$
\mathbb{A}_{ijkl}	Comp. of the 4 th order orient. tensor $\langle a_{ij} a_{kl} \rangle$
λ_i	Fabric eigenvalue of \mathbf{A}
\mathbf{V}	Matrix of eigenvectors of \mathbf{A}
ϕ	Zenith angle
θ	Azimuth angle
δ_{ij}	Kronecker delta symbol
S_2	Unit sphere
σ	A standard deviation
S_{ij}	Stress tensor
\mathcal{B}	Bingham distribution (4)
\mathbf{L}	Diagonal concentration matrix of \mathcal{B}
\mathcal{D}	Dinh-Armstrong distribution (3)
\mathbf{R}	Parameter matrix of \mathcal{D}
\mathcal{F}	Lliboutry distribution (1)
\mathcal{W}	Watson distribution (2)
κ	Scalar concentration parameter for \mathcal{F}
η	Scalar concentration parameter for \mathcal{W}

26 another (Glen and Perutz 1954, Durand and others 2008. After enough progressive rotation, the subgrains are considered to be
 27 separate grains. Mainly in warm ice above -10°C , dynamic recrystallization is often active. Here, old, highly strained grains
 28 are consumed by new incipient grains with low dislocation density. Unlike the case of polygonization, the new grain does not
 29 necessarily have a c-axis orientation close to that of the old grains it consumes. Thus, this process can have a larger effect

30 on c-axis fabric than polygonization. Dynamic recrystallization tends to produce weak c-axis fabrics with large, interlocking
31 grains (Kamb 1973, Duval and others 2000).

32 It is common to approximate the unknown, true ODF with a parametric ODF (PODF), which can normally be fit to observed
33 fabric data. This reduces the number of parameters. PODFs are used in a number of applications. First, they can allow for
34 efficient computation of anisotropic viscosity in anisotropic flow models. Some PODFs can allow for analytical computation
35 of viscosity with certain assumptions (Pettit and others 2007). If analytical relations are not available, viscosity or other
36 properties as a function of PODFs with one or two parameters can also be efficiently incorporated into flow models with a
37 lookup table (Gillet-Chaulet and others, 2006).

38 In addition, assumption of a specific PODF can also be useful for fast approximate fabric evolution models. Several PODFs
39 have been introduced as analytical estimates of fabric under specific flow conditions (Staroszczyk and Gagliardini 1999,
40 Svendsen and Hutter 1996, Gagliardini and Meysonnier 1999, Gödert and Hutter 1998). However, Gagliardini and others
41 (2009) noted that these are special cases of the Dinh-Armstrong distribution (Dinh and Armstrong, 1984). This is a very
42 flexible distribution that does not assume axial symmetry. Any initially isotropic fabric which evolves due to c-axis rotation
43 from basal slip under homogeneous strain has this ODF. Gillet-Chaulet and others (2006) developed a fast numerical fabric
44 evolution model based on the assumption of this PODF, which was coupled to an anisotropic ice flow model.

45 Recently, Maurel and others (2015) found analytical relationships of sonic velocity in ice as a function of c-axis fabric for
46 several PODFs. These relations were used by Smith and others (2017) to estimate fabric from microseismic signals in the
47 Rutford Ice Stream, yielding fabric estimates over a much larger region than can practically be done with ice-core thin-section
48 measurements of c-axes.

49 Aside from the analytically motivated PODFs mentioned previously, other PODFs have been introduced based on heuristic
50 considerations (e.g. Thorsteinsson 2002, Lliboutry 1993). More recently, Kennedy and others (2013) introduced the axially-
51 symmetric Watson distribution for use as a PODF. Most previously proposed PODFs exhibit axial symmetry, which is valid
52 only for single maximum or symmetric girdle fabrics. For a complete overview of this topic, see Gagliardini and others (2009).

53 In this paper, we propose the non axially-symmetric Bingham distribution as a more flexible PODF, motivated primarily by
54 statistical considerations. The Bingham distribution is a generalization of the Watson distribution. It can fit partial girdle
55 fabrics or asymmetric girdle fabrics often seen in ice cores. This makes the Bingham distribution applicable to a wider range
56 of commonly observed ODFs in comparison to axially-symmetric distributions.

57 Sampling error can be significant when inferring bulk properties (properties averaged over longer length-scales) of ice from a
58 small thin-section sample. When estimating a statistic from a limited sample, the sampling error is the error due to estimating
59 the statistic from a limited sample-size rather than the entire population that the sample was drawn from. C-axes from

60 thin-section samples can be assumed to be drawn from some unknown, underlying ODF (which may vary in space). Inferring
 61 information of the underlying ODF from a limited sample is therefore subject to sampling error. Correlations between c-axis
 62 measurements will tend to result in larger sampling error. Such correlations can occur, for example, due to polygonization
 63 (Durand and others, 2008) or the presence of strain heterogeneities.

64 Thorsteinsson (2002) found that approximately 5000 equally-sized grains are needed to effectively eliminate sampling error in
 65 a model of fabric evolution in response to applied homogeneous stress. This model includes nearest-neighbor stress interactions,
 66 so that nearby orientations are not independent. Later, Durand and others (2006) fit a quadratic estimate of the sampling
 67 error of the second-order orientation tensor (c.f. Table 1) by generating an array of fabric samples of 10,000 grains each from
 68 a PODF, and resampling from these fabrics. Unfortunately, this method is not directly applicable to per-pixel measurements,
 69 such as with electron backscatter diffraction or automatic fabric analyzers, since it does not take into account the correlation
 70 of nearby measurements. Here, we introduce an analytical estimate for the sampling distribution of fabric eigenvalues and
 71 eigenvectors based on data taken from a discrete thin-section sample, with either equal weighting of grains, or weighting by
 72 area. In most situations, area weighting should be preferred over equal weighting (Gagliardini and others, 2004). Everything
 73 else being equal, larger grains have a greater influence on rheological characteristics. Our analytical method is simple and
 74 makes no assumption on the form of the underlying ODF, which is usually unknown. We also develop approximations to
 75 account for intergranular covariances between c-axis measurements. Such covariances may be significant in many situations
 76 due to the presence of polygonization or small-scale deformation heterogeneities.

77 When fabric eigenvectors and eigenvalues are derived using area weighting of crystals in thin sections, we show that sampling
 78 error can be greatly increased. We also numerically derive sampling error estimates of estimated scalar enhancement factor
 79 (Lile, 1978) under simple shear from thin sections, where the enhancement factor is determined using the relations developed
 80 by Azuma (1995).

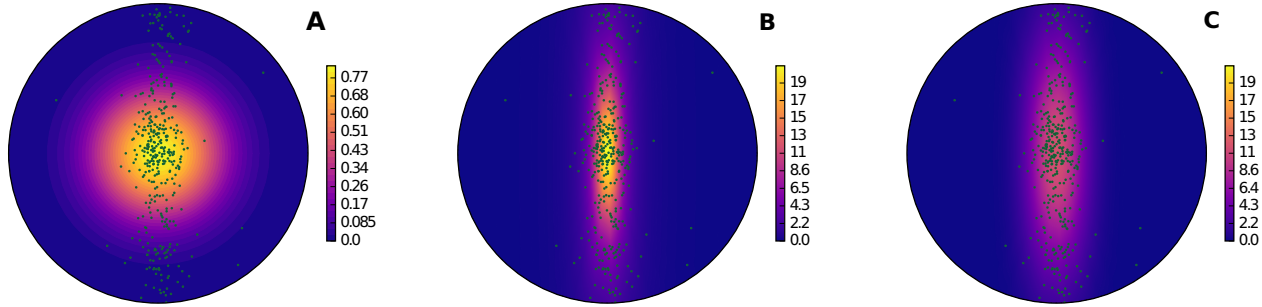
81 METHODS

82 In this section, we examine the usage of several PODFs. We also introduce methods of estimating sampling error in thin-section
 83 measurements through analytical and bootstrap techniques. Lastly, we introduce a bootstrap method of estimating uncertainty
 84 of enhancement factor in simple shear.

85 We will make extensive use of index notation in this paper, due to the use of higher-order tensors. However, at times we
 86 will not follow the summation convention for notational convenience (this is noted when it occurs). In addition, throughout
 87 this paper, the x direction will be associated with index 1, y with an index 2, and z with index 3.

88 ODFs are often summarized using orientation (or, moment) tensors (e.g. Svendsen and Hutter 1996). The component of the
 89 second-order orientation tensor A_{ij} is the expectation $\langle \hat{c}_i \hat{c}_j \rangle$, where $i, j = 1, 2, 3$. Here, \hat{c}_i is a random variable that c-axis

Fig. 1. Equal-area Schmidt plots of c-axis density for maximum-likelihood estimates of the Lliboutry distribution (A), the Dinh-Armstrong distribution (B), and the Bingham distribution (C) fitted to the 2905m thin section from the WAIS Divide ice core. The plots are oriented such that a c-axis lying along the fabric eigenvector associated with λ_3 is in the center of the Schmidt plot, and a c-axis lying parallel to the fabric eigenvector associated with λ_3 is oriented at the top or bottom of the figure, with respect to the page. C-axis measurements from the thin section are indicated by dots. Note that the density scale is the same in B and C, but differs in A. The Lliboutry distribution (1) fits the observed c-axes poorly, due to the assumption of axial symmetry. The Bingham distribution (4) and Dinh-Armstrong distribution (3) perform nearly equally well, but the Bingham distribution (4) produces a blunter maximum.



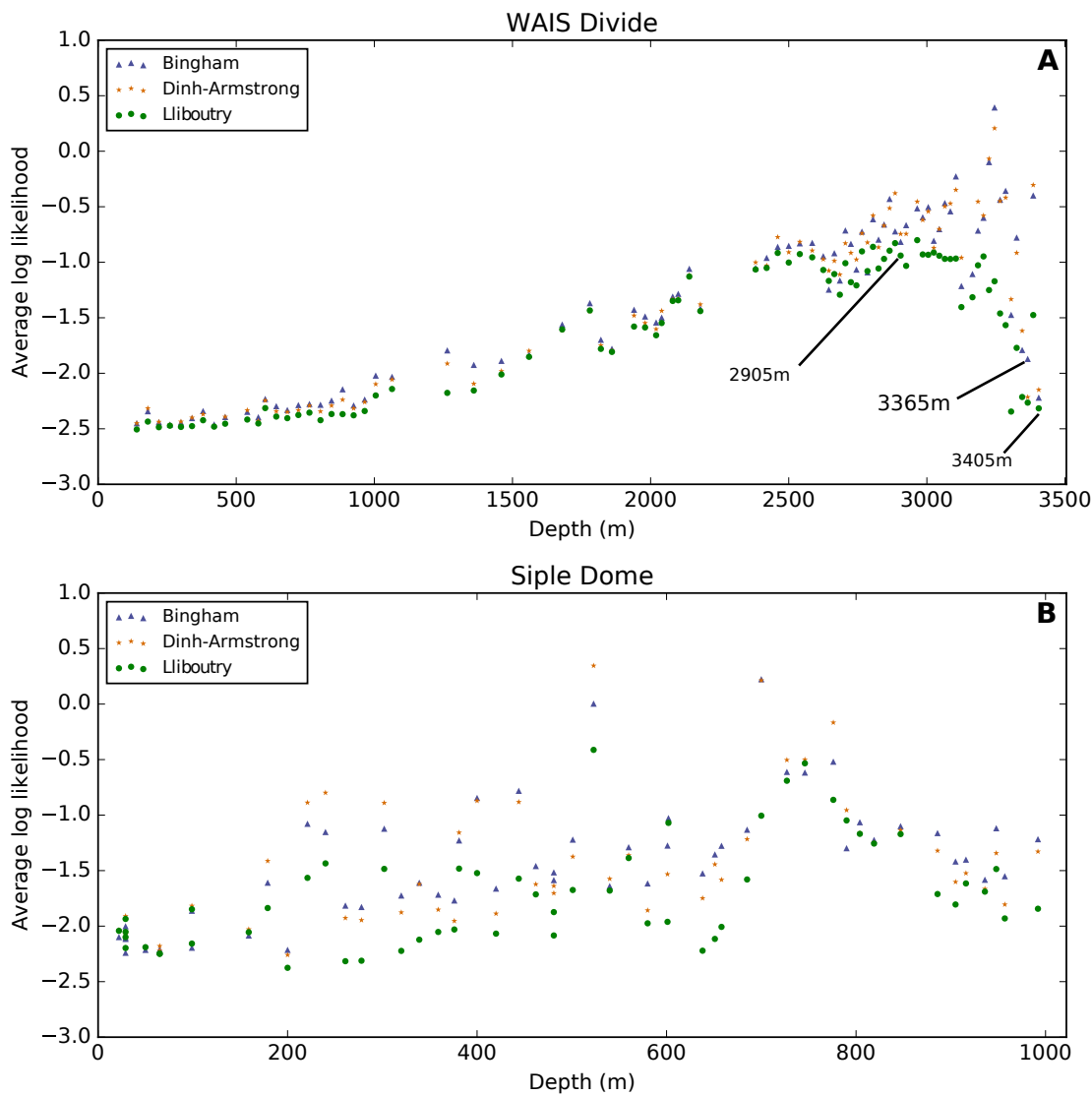
samples \tilde{c}_i are drawn from. The mean of the ODF, $\langle \hat{c}_i \rangle$, is always zero because of antipodal symmetry. Therefore, A_{ij} is also the covariance matrix of the distribution, by definition of covariance as $\text{Cov}(\hat{c}_i, \hat{c}_j) = \langle (\hat{c}_i - \langle \hat{c}_i \rangle)(\hat{c}_j - \langle \hat{c}_j \rangle) \rangle$. The diagonal elements A_{11} , A_{22} , and A_{33} give a measure of the c-axis concentration on the x , y , and z axes, respectively. Similar to the second-order orientation tensor, the fourth-order tensor is the expected value of the outer product of the c-axis with itself four times, whose components are given by $A_{ijkl} = \langle \hat{c}_i \hat{c}_j \hat{c}_k \hat{c}_l \rangle$. Since ODFs over the sphere are antipodally symmetric, odd-order tensors are zero.

The symmetric second-order orientation tensor may be decomposed into non-negative eigenvalues and three orthogonal eigenvectors. The eigenvalues of \mathbf{A} sum to unity by construction. The eigenvectors, or fabric principal directions, denote the directions of greatest density (corresponding to the largest eigenvalue), smallest density (the smallest eigenvalue), and a direction orthogonal to the other two. An isotropic fabric has three equal eigenvalues. A girdle fabric (in which there is a band of high concentration along a great circle) has two nearly equal eigenvalues, and one small eigenvalue. A single-maximum fabric has one large eigenvalue, and two small ones.

Parameterized orientation-density functions (PODFs)

We now examine the use of PODFs. We discuss several previously used PODFs which we consider to be especially statistically and physically plausible: the Fisher-type distribution introduced by Lliboutry (Lliboutry, 1993), the Watson distribution (Kennedy and others, 2013), and the Dinh-Armstrong distribution (Gillet-Chaulet and others, 2006). We also introduce the Bingham distribution (Bingham, 1974) as a PODF.

Fig. 2. Log-likelihood (with base e) of maximum-likelihood fits of the Dinh-Armstrong (3), Bingham (4), and Lliboutry (1) distributions to WAIS (A) Siple Dome (B) thin-sections. Higher log-likelihood indicates a better fit. The likelihoods are normalized by grain area for WAIS. For Siple Dome, they are normalized by the number of grains. The Dinh-Armstrong and Bingham distributions perform similarly, with the Lliboutry distribution having lower likelihood for almost all thin sections. In thin-sections near the top of both cores all three distributions perform similarly, with lower average log-likelihood of around -2 to -2.5. These thin sections are closer to isotropy, which all three distributions are capable of representing exactly with average log-likelihood of $\ln(1/(4\pi)) \approx -2.53$ for any observed ODF. For all distributions, the highest average log-likelihoods are reached for highly concentrated single-maximum fabrics. The thin section at 2905m (Figure 1), and the multiple maximum thin sections at 3365m and 3405m are indicated.



107 Lliboutry and Watson distributions

Lliboutry (1993) first suggested the use of an axially-symmetric Von Mises-Fisher type distribution defined over the half sphere, which we will refer to as the Lliboutry distribution. Expressed in a reference frame where the vertical axis is aligned with the

symmetry axis, this is,

$$\mathcal{F}(\phi|\kappa) = \frac{\kappa \exp(\kappa \cos(\phi))}{e^\kappa - 1}, \quad (1)$$

where ϕ is the zenith angle, and κ is a scalar concentration parameter. Gagliardini and others (2009) found that this distribution provided the best fit for fabric in a thin section from the Dome C core. As a modification to the Lliboutry distribution, Kennedy and others (2013) introduced the Watson distribution as a PODF, which is defined over the whole sphere:

$$\mathcal{W}(\phi|\eta) = a \exp(\eta \cos^2(\phi)), \quad (2)$$

108 where η is a concentration parameter, ϕ is the zenith angle, and a is a normalization constant. With the axis of symmetry
 109 parallel to the eigenvector associated with the largest eigenvalue, the Lliboutry distribution can represent single-maximum
 110 fabrics with a positive concentration parameter, and the Watson distribution can do the same with a negative concentration
 111 parameter. Likewise, girdle fabrics can be represented with a positive concentration parameter for the Watson distribution,
 112 and a negative concentration parameter for the Lliboutry distribution, with the axis of symmetry parallel to the eigenvector
 113 associated with the smallest eigenvalue. The Watson distribution has the important advantage of being antipodally symmet-
 114 ric. Because individual ice-crystal c-axis orientations cannot be distinguished between \mathbf{c} and $-\mathbf{c}$, any PODF defined on the
 115 sphere should also be antipodally symmetric. It is common practice to define PODFs only on the upper hemisphere. Any
 116 PODF defined on the upper hemisphere can trivially be extended to the whole sphere. For the Lliboutry distribution (1), the
 117 derivative of density with respect to ϕ does not vanish at the equator when extended over the whole sphere. The derivative
 118 is then discontinuous at the equator. The discontinuity does not have a physical basis. This same difficulty appears when
 119 extending any distribution on the half to the full sphere whose density gradient does not vanish at the equator.

120 The Dinh-Armstrong distribution

We now examine another distribution, which we will refer to as the Dinh-Armstrong distribution (Dinh and Armstrong, 1984).

This is given by,

$$\mathcal{D}(\mathbf{c}|\mathbf{R}) = \frac{1}{(\mathbf{c}^T \mathbf{R} \mathbf{c})^{\frac{3}{2}}}, \quad (3)$$

121 where \mathbf{R} is a symmetric second-order tensor with a determinant of unity. Gillet-Chaulet and others (2006) introduced this
 122 distribution to glaciology for fabric evolution. If \mathbf{c} rotates due only to slip on the basal plane, and if the ODF was at one time
 123 isotropic, then the ODF has this distribution with $\mathbf{R} = \mathbf{FF}^T$, where \mathbf{F} the bulk deformation gradient. In the reference frame
 124 defined by the fabric principal-directions, \mathbf{R} is a diagonal matrix, with diagonal entries r_i . The three elements r_i possess only
 125 two degrees of freedom, due to the constraint that the determinant is unity. The Dinh-Armstrong distribution is a special
 126 case of the angular central Gaussian (ACG) distribution (Tyler, 1987), where the matrix \mathbf{R} has a determinant of unity. The

- 127 ACG distribution is the distribution of angles of a multivariate normal distribution: Suppose that a random vector $\hat{\mathbf{x}}$ possesses
 128 a multivariate normal distribution centered at zero. Then, the unit vector $\hat{\mathbf{x}}/\|\hat{\mathbf{x}}\|$ is distributed by ACG distribution. The
 129 Dinh-Armstrong distribution can be fitted with only \mathbf{A} .

130 *The Bingham Distribution*

We now introduce the Bingham distribution (Bingham, 1974) as a generalization of the Watson distribution (2). The density, in Cartesian coordinates, is

$$\mathcal{B}(\mathbf{c}|\mathbf{V}, \mathbf{L}) = \gamma(\mathbf{L}) \exp(-\mathbf{c}^T \mathbf{V} \mathbf{L} \mathbf{V}^T \mathbf{c}), \quad (4)$$

- 131 where \mathbf{V} is the matrix of eigenvectors of the second-order orientation tensor \mathbf{A} , and γ is a normalization constant. Also, \mathbf{L} is
 132 a diagonal matrix containing three concentration parameters ι_i such that $\iota_1 < \iota_2, \iota_3$. This distribution is invariant for changes
 133 in the sum of concentration parameters, because any change in the sum of concentration parameters is negated by a change in
 134 the normalizing constant $\gamma(\mathbf{L})$. Because of this, we may set $\iota_1 = 0$, since if the parameters are ι_i , with $\iota_1 \neq 0$, the distribution
 135 with concentration parameters $\iota_i - \iota_1$ is identical. This reduces the number of free parameters from three to two. If we set
 136 $\iota_2 = 0$ as well, the Watson distribution (2) is recovered. This distribution has a number of desirable properties. It is able to
 137 represent single-maximum fabric and girdle fabrics, but is also able to capture fabrics with three distinct eigenvalues, such as
 138 partial girdles, or girdles that are concentrated in one direction.

139 In addition, the Bingham distribution is parsimonious: If we seek a PODF to fit a measured \mathbf{A} , the Bingham distribution is
 140 the simplest hypothesis that fits the observed data. It avoids introducing spurious structures that are unnecessary to satisfy
 141 the assumption of a particular value of \mathbf{A} . Specifically, the Bingham distribution is the maximum-entropy distribution for any
 142 spherical distribution with a given second-order orientation tensor (or, covariance matrix) (Mardia, 1975).

143 Distributional entropy is defined similarly to Gibbs entropy in thermodynamics. The entropy of a probability distribution
 144 q is the expectation $< -\ln q >$. Distributions that have high entropy contain less information. Thus, when selecting a para-
 145 metric distribution, the distribution with the highest entropy that adequately fits the given data is the most parsimonious
 146 explanation of the observations. In this sense, the Bingham distribution is similar to the multivariate normal distribution,
 147 which has maximum entropy of any distribution over n-dimensional Euclidean space possessing a given covariance matrix, or
 148 the exponential distribution, which has the maximum entropy of any distribution on the line with a given mean. The Bingham
 149 distribution is in fact the multivariate normal distribution with zero mean conditioned to lie on the unit sphere. Therefore, it
 150 has a direct relationship to the Dinh-Armstrong distribution (3).

151 The Bingham distribution has found use in paleomagnetics (Onstott, 1980) and other fields. Its wider adoption has been
 152 hampered by a lack of closed-form analytical expressions for the normalization constant and the maximum-likelihood estimator

153 of ι_i given the data, necessitating a greater use of slower numerical methods than many other distributions. However, this is
 154 not as great of a challenge as it once was. In addition, since the distribution is determined by two parameters, it is amenable
 155 to methods based on lookup tables.

156 SAMPLING ERROR IN THIN SECTIONS

157 We now develop analytical and bootstrap estimates of sampling error of inferring the second-order orientation tensor of the
 158 true ODF that the limited thin-section sample is assumed to be drawn from. Several different methods have been developed
 159 to measure c-axes in thin sections. The Rigsby Stage technique (Langway, 1959) was the first method for c-axis determination
 160 in ice thin sections, using extinction angles of polarized light. This is a manual technique which gives per-grain measurements
 161 of c-axes. In recent years, automatic fabric analyzers (Wilen and others, 2003) and electron-backscatter diffraction (EBSD)
 162 (Iliescu and others, 2004) have become popular. These techniques yield high-resolution images of grain orientations, with
 163 c-axes measured per-pixel, rather than per-grain. Typically, there are many more pixels than grains. It may initially seem
 164 that the sampling error would be nearly eliminated, due to the very large number of pixels. However, in Appendix A1 we
 165 show this is not the case, because nearby pixels are usually highly correlated. We will also show that intragrain variability of
 166 c-axis orientations may be neglected when estimating sampling error from thin sections. From these two results, we show that
 167 sampling error of \mathbf{A} inferred from per-pixel measurements is similar to that of per-grain measurements.

168 We briefly review some concepts of independence and correlation in the context of thin-section fabric measurements. Two
 169 events (for example, c-axis measurements from a thin section) a and b are said to be independent if they carry no information
 170 about one another: the probability of observing b given the observation of a is equal to the probability of observing b without
 171 having observed a . For example, two rolls of a die are independent. The probability of getting a three on the second roll is
 172 unaffected by the side the first roll lands on. Note that this notion of independence is unrelated to whether the die is fair or
 173 not (or any distributional assumption). If, for example, it lands on the three side 95% of the time, the first roll coming up a
 174 three does not affect the chances of the second roll coming up a three: The chance of a three on the second roll is still 95%.

175 Correlation is a related concept. The correlation of two random variables is the ratio of their covariance to the product of their
 176 standard deviations. Correlation and covariance between independent variables is always zero, no matter what distribution
 177 they are drawn from. However, zero correlation does not necessarily imply independence.

178 Spatial correlation of c-axis orientations may occur, for example, due to polygonization: if progressive subgrain rotation
 179 splits apart a grain, the two resulting grains will have similar orientation. This results in spatial correlation between grain
 180 orientations. Correlation between c-axis measurements is not closely related to the distribution of c-axis orientations. Suppose
 181 two measurements were drawn from a vertical single-maximum fabric. The two measurements may be closely aligned, since
 182 most c-axes in vertical single-maximum fabrics are near vertical. However, this does not imply that they are correlated. They

183 are only correlated if knowledge of the first measurement gives additional information on the second measurement. This is
 184 similar to the previous analogy of unfair dice.

185 We do not consider bias in inferring larger-scale fabric from thin sections due to spatial variability in the ODF. For example,
 186 near the bed of the WAIS Divide ice-core, there are alternating layers of dynamically recrystallized ice (with weaker fabric)
 187 and non-dynamically recrystallized ice (possessing stronger fabrics). A thin-section sample taken from the stronger fabric may
 188 be a representative sample of the ODF averaged over the small length-scale of that layer at the thin-section site. However, it
 189 would be a very poor estimate of the fabric averaged over longer length-scales (including other layers). Thus, it would be an
 190 inappropriate fabric estimate to use for an ice flow model with cell sizes in the tens of meters.

191 As another example, Alley and others (1997) observed regions or “stripes” of non-vertical c-axis fabric disrupting otherwise
 192 vertical-maximum fabric in the GISP2 core. Suppose a thin section is intersected by single stripe. We may estimate A_{ij} from
 193 this particular thin section. However, a thin section taken a few centimeters away could be intersected by two stripes, or no
 194 stripes at all. Again, this introduces a bias distinct from sampling error when interpreting fabric averaged over larger length
 195 scales: the thin section is not representative of the fabric averaged over stripes and the background vertical-maximum fabric.

In Appendix A, we derive an estimate (A8) of the variance of the random variable $\hat{\mathbf{A}}$ that the sample estimate $\tilde{\mathbf{A}}$ of the
 bulk second order orientation tensor \mathbf{A} is assumed to be drawn from. This estimate can include treatments of intergranular
 covariances, if necessary. This estimate is appropriate for both per-pixel and per-grain c-axis measurements. From (A8) and
 (A6), in the special case where intergrain correlations are negligible, and under the assumption that all measurements are
 identically distributed, we may estimate the variance of $\tilde{\mathbf{A}}$ in terms of estimated second- and fourth-order orientation tensors
 as,

$$\text{Var}(\hat{A}_{ij}) \approx s_{ij}^0 s_n^2 \approx \left(\tilde{\mathbb{A}}_{ijij} - \tilde{A}_{ij} \tilde{A}_{ij} \right) s_n^2, \quad (5)$$

196 with no sum in i or j . Here, s_{ij}^0 is the sample variance of the measured component of the structure tensor $\tilde{a}_{ij} = \tilde{c}_i \tilde{c}_j$ taken
 197 over the thin section. The scalar s_n^2 is the sum of squared normalized grain weights. The estimate (5) applies whether the
 198 data are collected per-grain, as with manual fabric measurements, or per-pixel. We show in the appendix that intragranular
 199 misorientations can reasonably be ignored when estimating sampling error; thus per-pixel measurements can be averaged out
 200 for each grain for the purposes of estimating sampling error. When per-pixel measurements are averaged within each grain, the
 201 variance estimate is similar to the estimate if the data were collected on a per-grain basis in the first place, if the proportion
 202 of measurements within each grain is proportional to grain area.

In the appendix, we also derive estimates of sampling variance for sample fabric eigenvalues and eigenvectors under the
 assumption that formulas for first-order eigenvalue and eigenvector perturbations are approximately valid. The estimated
 variances of eigenvalue estimates $\tilde{\lambda}_i$ are given by estimated variances of the diagonal elements \hat{A}_{ii} (5) in the reference frame

defined by the eigenvectors of $\tilde{\mathbf{A}}$. In the same reference frame, the variance of the sample estimate of the matrix of fabric eigenvectors can be estimated as,

$$\text{Var}(\tilde{\mathbf{V}}) = \begin{pmatrix} 0 & \frac{\text{Var}(\hat{A}_{12})}{(\tilde{\lambda}_2 - \tilde{\lambda}_1)^2} & \frac{\text{Var}(\hat{A}_{13})}{(\tilde{\lambda}_3 - \tilde{\lambda}_1)^2} \\ \frac{\text{Var}(\hat{A}_{21})}{(\tilde{\lambda}_1 - \tilde{\lambda}_2)^2} & 0 & \frac{\text{Var}(\hat{A}_{23})}{(\tilde{\lambda}_3 - \tilde{\lambda}_2)^2} \\ \frac{\text{Var}(\hat{A}_{31})}{(\tilde{\lambda}_1 - \tilde{\lambda}_3)^2} & \frac{\text{Var}(\hat{A}_{12})}{(\tilde{\lambda}_2 - \tilde{\lambda}_3)^2} & 0 \end{pmatrix}, \quad (6)$$

where $\tilde{\lambda}_i$ is the sample estimate of the fabric eigenvalue λ_i . The three elements above the diagonal also give a first-order estimate of the sampling variance of the Euler angles of the fabric eigenvectors. The estimated variance of the rotation angle about each axis are given by $\text{Var}(\hat{V}_{12})$ for the z -axis, $\text{Var}(\hat{V}_{13})$ for the y -axis, and $\text{Var}(\hat{V}_{23})$ for the x -axis.

From this, variance of the Euler angle about an axis is inversely proportional to the square of difference in the fabric eigenvalues associated with the other two axes. This means that the variance becomes large if the other two eigenvalues are very close together. It is not defined if the eigenvalues are identical. This is because if there are two identical eigenvalues, then there are two corresponding orthogonal eigenvectors, and any vector in the plane formed by those eigenvectors is an eigenvector as well. Therefore, there is not a unique reference frame which makes \mathbf{A} diagonal in this case.

Grain-size distribution also has an important influence on sampling error of eigenvalue and eigenvector estimates. Uneven distributions, in which a small number of large grains account for most of the volume, induce greater sampling uncertainty than a grain-size distribution of more evenly-sized grains. As an extreme example, if a fabric thin section contains one large grain, and a thousand infinitesimally small grains, the sample size is effectively one grain, because the small grains have weightings close to zero. The estimated variance of \hat{A}_{ij} is proportional to the sum of squared normalized weights, s_n^2 . For a fixed number of grains, this attains a minimum value for equal normalized weights. Grain-size distributions found in ice cores often have a few large grains and many small grains. Equal weighting can therefore lead to a significant underestimate of sampling error.

Bootstrap estimates of sampling error

We now explore the use of bootstrap resampling for estimating fabric sampling error. Bootstrapping (Efron, 1992) is based on the idea that the empirical distribution of the observed data can be used as an approximation to the unknown true distribution. This requires that the data are approximately independent and are drawn from the same distribution. We can approximate the distribution of a statistic of interest that depends on the data by first resampling the empirical distribution many times, with replacement. The statistic is calculated for each resample, thus approximating the distribution of the statistic. In the case of per-grain c-axis measurements, this is straightforward, assuming that orientations of different grains are approximately independent.

Bootstrapping is not valid for resampling per-pixel measurements (with many pixels per grain) because of the high correlation of the c-axis orientations of nearby points within the same grain. The general idea of bootstrapping is that it is supposed

228 to approximate repeated draws from the underlying distribution by resampling from the original sample. However, this does
 229 not work when the data are dependent, as is the case with per-pixel c-axis measurements. The data depend on one another,
 230 in that if we observe a pixel with a particular orientation, many other nearby pixels are likely to have the same orientation,
 231 conditioned on the first pixel. They are not sampled independently from the ODF. Simply resampling all data from a thin
 232 section ignores spatial correlation of the data, leading to a large underestimate of variance.

233 Instead, we suggest a technique known as block bootstrapping (Hall and others, 1995). Block bootstrapping resamples blocks
 234 of data at a time, rather than individual data. The goal is that the larger blocks are approximately uncorrelated. There is a
 235 trade-off involved in choosing block sizes: larger blocks have less correlation with each other, which helps avoid underestimating
 236 variance. However, using blocks that are too large causes overestimation of the variance by making the effective sample size
 237 too small. Ideally, the variance within each block should be as small as possible, while maintaining approximate independence
 238 between blocks. An obvious choice for thin sections is to take individual grains as blocks: Within-block variance is small, since
 239 c-axes within a grain are not misoriented by more than several degrees (larger misorientations are usually taken to be separate
 240 grains). If intergrain covariance is small enough, they can be assumed to be approximately independent. By taking individual
 241 grains as blocks, block bootstrapping uncertainties of per-pixel c-axis measurements is identical to ordinary bootstrapping of
 242 per-grain c-axis measurements. Unfortunately, covariances between grains are difficult to include with this method.

243 Sampling error in enhancement factor estimates

244 Sampling error in fabric may lead to significant uncertainties in flow characteristics. In this section, we develop a bootstrap
 245 estimate of the sampling distribution of an estimate of enhancement factor derived from thin sections. This should not be
 246 interpreted as a rigorous estimate of uncertainty in enhancement factor, but solely as an illustration of how uncertainty in
 247 fabric could translate into uncertainty of flow characteristics.

248 The Schmid factor is a measure of the proportion of compressive stress resolved on a c-axis basal plane. It is given by
 249 $S_g = \cos \chi \sin \chi$, where χ is the angle between the c-axis and the stress axis. Azuma (1995) found that the scalar enhancement
 250 factor of the coefficient of Glen's flow law under uniaxial compression is approximately proportional the fourth power of the
 251 Schmid factor averaged among grains. This assumption is also used for the CAFFE flow model (Placidi and others, 2010).
 252 The dependence on the fourth power indicates that smaller variations in c-axis fabric can induce much larger changes in
 253 deformation rates.

254 A bootstrapping technique for estimation of the sampling error of estimated enhancement factor can be easily derived under
 255 the assumption that the measured per-grain c-axis orientations are independently and identically distributed. Grain c-axis
 256 orientations from a thin-section sample are repeatedly resampled with replacement. For each resample, the enhancement factor
 257 is found from the fourth power of the average Schmid factor, scaled by the average Schmid factor of an isotropic crystal, which

258 is 1/3. This scaling is chosen to give isotropic ice an enhancement factor of unity. The set of enhancement factors derived
 259 from each resample is then an estimate of the sampling distribution of the estimated enhancement factor. In the next section,
 260 we apply this technique to estimate sampling error for the estimated enhancement factor under shear for the WAIS Divide
 261 thin-section data.

262 RESULTS AND DISCUSSION

263 In this section, we evaluate the PODFs introduced previously using thin-section c-axis measurements from the WAIS Divide
 264 (Fitzpatrick and others, 2014) and Siple Dome (Wilen, 2002) ice cores. We also give estimates of fabric eigenvalue and
 265 eigenvector sampling error of thin sections in the WAIS using the previously developed analytical and bootstrap methods.
 266 Lastly, we show estimates of the sampling error of estimated enhancement factor from thin sections at the WAIS Divide ice
 267 core.

268 Characteristics of WAIS Divide and Siple Dome fabric measurements

269 The WAIS Divide core site is 24 km from a saddle of the West Antarctic Ice Divide. The ice experiences longitudinal extension
 270 along the flow direction, as is typical in accumulation areas. Because the ice divide is curved into a saddle, flow lines also
 271 converge laterally, producing horizontal compression transverse to the flow direction (Conway and Rasmussen 2009, Kluskiewicz
 272 and others 2017). Deeper in the ice, simple shear becomes important. These flow characteristics are reflected in the fabric. In
 273 the top 2500m of the 3505m deep core, girdle fabrics with c-axes concentrated towards vertical predominate. This is due to
 274 extension occurring in the direction orthogonal to the axis of the divide. Below this, vertical maximum fabrics dominate due
 275 to increased shearing (Fitzpatrick and others, 2014). Near the bottom of the core, some thin sections display coarse-grain,
 276 weaker fabrics due to dynamic recrystallization. The thin sections at 3365m and 3405m display multiple maxima. However,
 277 since these thin sections have coarse-grained ice, with only several dozen grains, the apparent multiple maxima may be an
 278 artifact of small sample size (Fitzpatrick and others, 2014).

279 The Siple Dome ice core is 992m deep. The top 700m of the core is characterized by weak girdle fabrics, with a greater
 280 concentration of c-axes near vertical. This may reflect the presence of both vertical compression and horizontal tension in a
 281 similar manner to WAIS Divide (Gow and Meese, 2007). Below this, single maximum fabrics appear. Near the bottom of the
 282 core, dynamic recrystallization becomes more active, producing very coarse grained, weak fabrics (Gow and Meese, 2007).

283 Comparison of PODFs

284 We now compare the Dinh-Armstrong distribution (3), the Lliboutry distribution (1), and the Bingham distribution (4) using
 285 thin-section data from the WAIS Divide ice core (Fitzpatrick and others, 2014) and the Siple Dome ice core (Wilen, 2002).
 286 We do this by comparing log-likelihoods of maximum-likelihood fits of each distribution to each thin section. Comparing log-

287 likelihoods of data for the maximum likelihood fits of these distributions is a fair and quantitatively coherent way of comparing
 288 their performance. Maximum-likelihood estimation is a standard method of selecting a distribution to fit observed data. The
 289 distribution with the highest likelihood is, in a sense, the best distribution to explain the observed data.

290 The data likelihood of a parameter value ν of a parameterized distribution f_ν is the probability of those observed data
 291 arising under the distribution f_ν (with the parameter value ν). The maximum-likelihood value of ν is the value of ν that
 292 maximizes this likelihood. That is, the maximum-likelihood estimator maximizes $\text{Pr}(\mathbf{d}|\nu)$, where \mathbf{d} is the observed data. In
 293 practice, the log-likelihood is maximized instead of directly maximizing the likelihood.

Let \mathbf{c}^i be the c-axis measurement with index i from a thin-section sample with n measurements. For a PODF parameterized
 by ν , the average log-likelihood of a c-axis measurement under the maximum-likelihood fit is given by,

$$\mathcal{L}(\nu^*) = \sum_i w_i \ln \left(\text{Pr}(\mathbf{c}^i | \nu^*) \right), \quad (7)$$

294 where ν^* is the maximum-likelihood estimate ν based on the observed c-axis data. The factor w_i is the weight of measurement
 295 i : either $1/n$ if measurements are equally weighted, or the area of the grain, normalized such that the area of the thin section
 296 is unity. The log-likelihood of an entire thin section is dependent on the number of measurements. Comparing the normalized
 297 log-likelihood between thin sections removes this bias, allowing fits of different thin sections to be compared directly.

298 For the Bingham distribution (4), we computed the maximum-likelihood density estimates of \mathbf{L} numerically, given the
 299 observed grain orientations from the WAIS and Siple Dome ice-cores. For the Dinh-Armstrong distribution (3), we numerically
 300 found the maximum-likelihood estimates for the parameter \mathbf{R} . For the Lliboutry distribution (1) with a single-maximum fabric,
 301 we first rotated the reference frame into the fabric principal reference frame such that the eigenvector corresponding to the
 302 largest eigenvalue points vertical. For the Lliboutry distribution (1) with a girdle fabric, we rotated the reference frame such
 303 that the eigenvector associated with the smallest eigenvalue is vertical. We then numerically found the maximum-likelihood
 304 estimates for the concentration parameter κ .

305 In Fig. 1, we plot the densities of maximum likelihood estimates of all three distributions for the 2905m thin section from
 306 the WAIS Divide ice core. This thin section is a partial girdle fabric, with a highly elongated maximum. It is somewhat of a
 307 borderline case between a girdle fabric and a single-maximum fabric, with $\lambda_3 = 0.7$ and $\lambda_2 = 0.29$. The thin section is best
 308 fit by the Lliboutry distribution using a positive concentration parameter, yielding a single-maximum fabric, as opposed to a
 309 negative concentration parameter, yielding a symmetric girdle fabric. Here, the Lliboutry distribution (1) performs poorly. The
 310 assumption of axial symmetry cannot account for the elongated shape of the region of greatest c-axis concentration. Likewise,
 311 it would not be well fit by an axially-symmetric girdle distribution. The Dinh-Armstrong distribution (3), and Bingham
 312 distribution (4) perform similarly. The Bingham distribution (4) produces a blunter maximum.

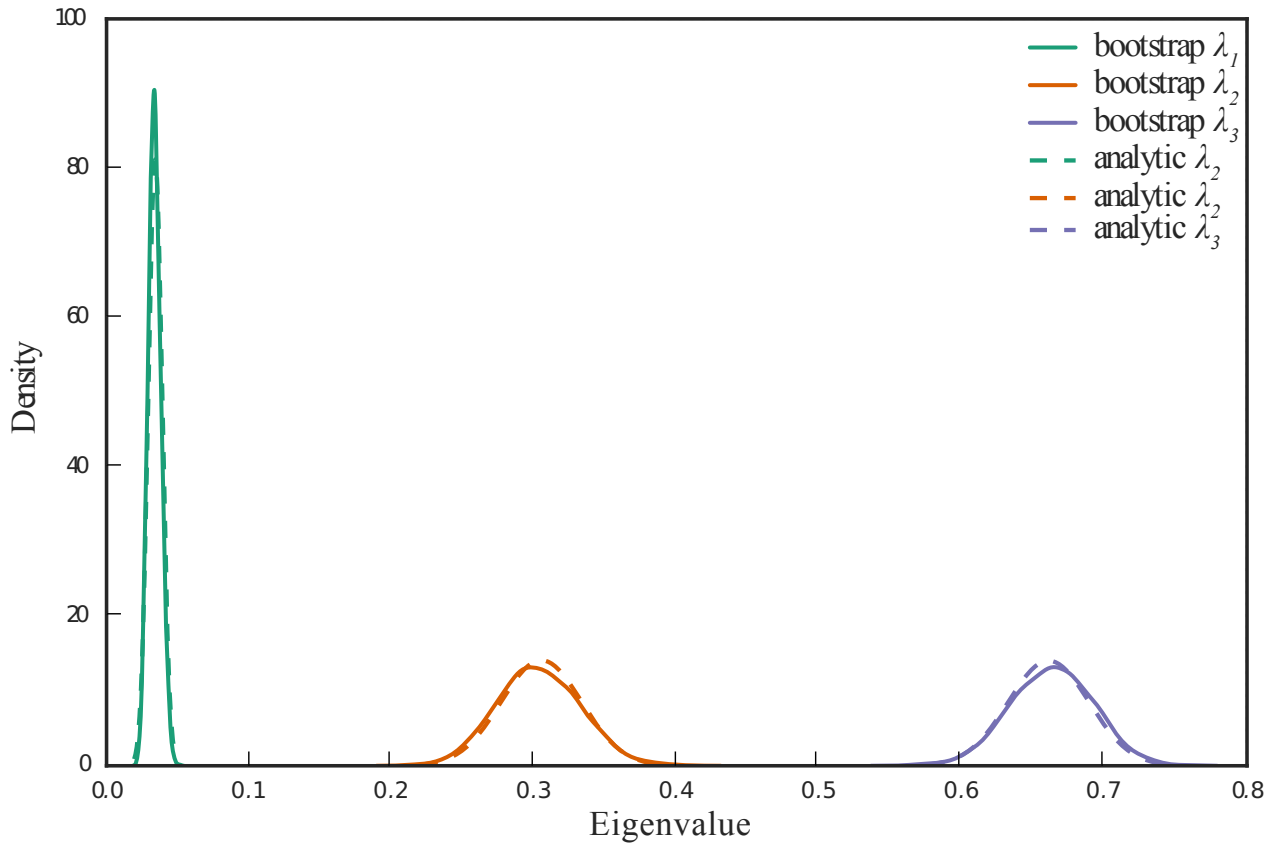
313 In Figure 2, we plot average log-likelihoods of the maximum likelihood estimates (with parameters \mathbf{L} , κ , and \mathbf{R}) of all three
 314 distributions for thin sections in the WAIS Divide and Siple Dome ice cores. We are not plotting the maximum-likelihood
 315 values of these parameterized distributions, because they themselves give no information on the goodness of fit. The average
 316 likelihood for each distribution is strongly affected by the fabric type. All three PODFs are capable of exactly representing
 317 isotropic fabrics, and in the limit, perfect single maximum fabrics. Log-likelihoods are usually lower for diffuse fabrics than
 318 for concentrated fabrics. In concentrated fabrics, most of the grains lie in orientation which have high ODF density, resulting
 319 in high likelihoods. In the limit of grains taken from a perfect single-maximum fabric, the log-likelihood of each grain is
 320 positive infinite. On the other hand, in the limit of an isotropic fabric, the unnormalized log-likelihood of every grain is always
 321 $-\ln(4\pi) \approx -2.53$. Likewise, the average log-likelihood of any set of c-axes is $-\ln(4\pi)$. This is because the area of the surface
 322 of the sphere is 4π .

323 The first 1000 m of the WAIS Divide core, and the top 150 m of the Siple Dome core are closer to isotropy, thus all three
 324 distributions perform similarly with average log-likelihoods of around -2 to -2.5. This is close to the average log-likelihood of
 325 approximately -2.53 for isotropic fabrics. Thin sections exhibiting stronger single-maximum fabrics below about 2500 m in
 326 the WAIS core have higher likelihoods for all three distributions. Weak recrystallized layers with apparent multiple maxima
 327 near the bottom of the WAIS core have lower likelihoods for all three distributions. The same is true of some recrystallized
 328 layers in the Siple Dome core. In the Siple Dome core, the Lliboutry distribution (1) fits thin sections between 300 m and 700
 329 m possessing girdle or partial-girdle fabrics rather poorly, likely due to its axial symmetry. Similarly, girdle and partial-girdle
 330 fabrics in the upper 2500 m of the WAIS ice core are poorly fit by the Lliboutry distribution (1).

331 The Lliboutry distribution (1) has the lowest log-likelihood for nearly all thin sections, because its assumption of axial
 332 symmetry is overly restrictive for most of these data. The Bingham (4) and Dinh-Armstrong (3) distributions perform similarly
 333 overall, with the Bingham distribution (4) slightly outperforming the Dinh-Armstrong distribution (3) overall. For these data
 334 as a whole, this indicates that the Bingham distribution (4) is the best choice due to its maximum-entropy property. However,
 335 the Dinh-Armstrong distribution (3) does not have a normalization constant that must be found numerically, as the Bingham
 336 distribution (4) does. Therefore, it may be a better choice for many applications.

337 In fitting the Bingham distribution (4) or Dinh-Armstrong distribution (3) to an observed fabric, only the second moment of
 338 the observed fabric, \mathbf{A} , is needed. Higher moments are neglected, which means that these cannot fit complex fabric distributions,
 339 such as those with multiple maxima. We are not aware of any proposed PODFs that can capture multiple maxima. However,
 340 defining complex PODF to fit multiple maxima or other complex distributions would become numerically unwieldy. For some
 341 current applications of PODFs, such distributions would also be less useful. For example, fabric inference from body-wave
 342 velocities are not able to infer multiple maxima or complex fabric features. With two shear-wave polarizations, along with

Fig. 3. Bootstrap resampling and analytical estimates of the sample distributions of the eigenvalues of the thin section fabric at the 1940m thin-section from the WAIS Divide core. The analytical (dashed lines) and resampled bootstrap estimates (solid lines) match closely.



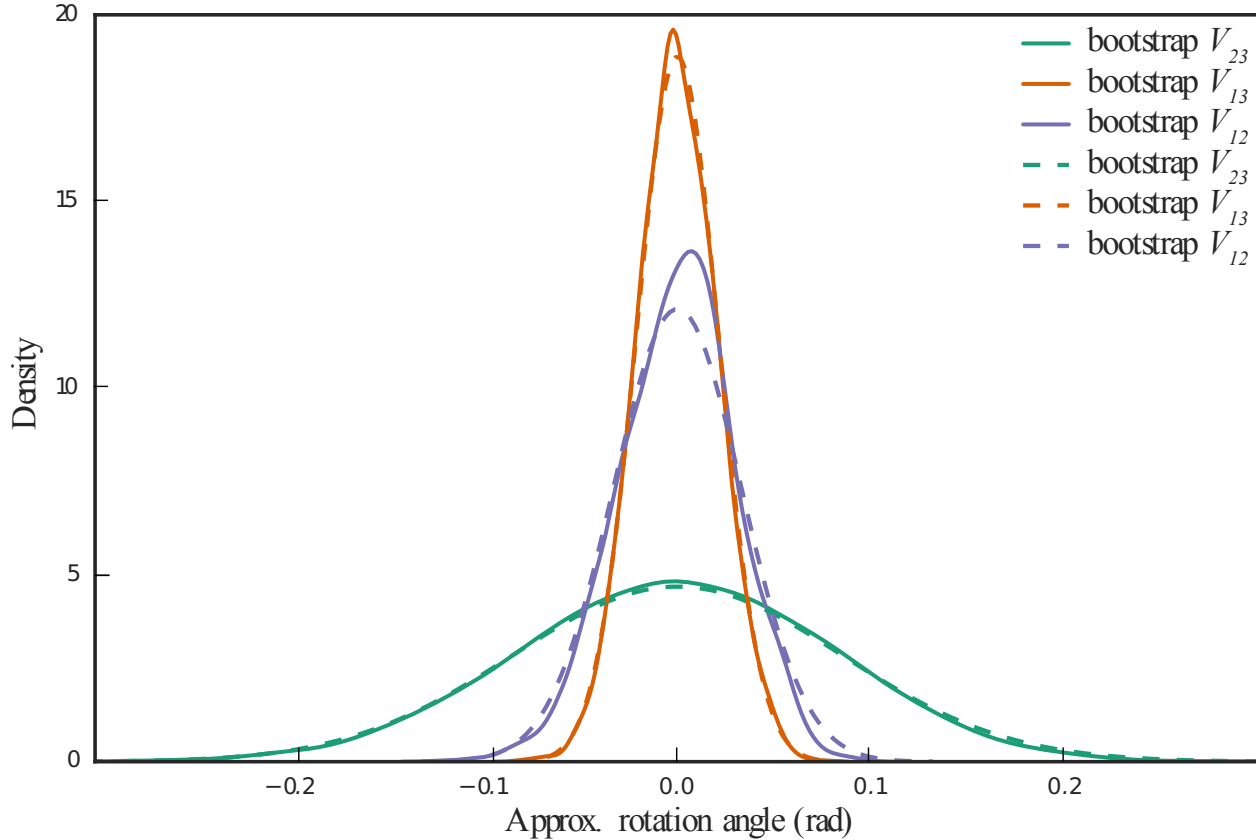
343 P-wave velocity, there are at most three degrees of freedom (e.g. Kluskiewicz and others 2017). Thus, it is impossible to fit
 344 distributions with more than three degrees of freedom with body-wave velocity data alone. More degrees of freedom could be
 345 fitted through measurement at multiple angles, or the use of interfacial wave velocities in boreholes, however.

346 In addition, if the goal is to estimate a bulk fabric distribution from a limited thin-section sample, more complex distributions
 347 would tend to overfit the data. For example, multiple-maxima fabrics are typically observed in very coarse grain ice, which
 348 yields thin-section samples with small numbers of grains. Trying to fit every grouping runs the risk of fitting random sampling
 349 variability. With these considerations, the Dinh-Armstrong (3) and Bingham (4) distributions provide a reasonable compromise
 350 between quality of fit, robustness to overfitting, and tractability.

351 Sampling-error estimates for WAIS Divide

352 We now derive error estimates for the WAIS Divide core using both the analytical method developed in the appendix, and
 353 bootstrapping. The c-axis measurements were collected on a per-grain basis (Fitzpatrick and others, 2014). We compare the

Fig. 4. Bootstrap resampling and analytical estimates of the sample distributions of the off-diagonal elements \hat{V}_{23} , \hat{V}_{13} , \hat{V}_{12} of the matrix \mathbf{V} formed by the fabric eigenvectors of the thin section fabric at 1940m, in the reference frame defined by the observed eigenvectors $\tilde{\mathbf{V}}$ of $\tilde{\mathbf{A}}$. To first order, these are the estimated sampling distributions of the Euler angles of rotation between the true eigenvectors and the sampled eigenvectors associated with eigenvalues λ_1 , λ_2 , and λ , respectively.



354 derived sampling distribution of fabric eigenvalues from both approaches in Figure 3. To assess uncertainty in fabric principal
 355 directions, we also compare the sampling distributions of the fabric Euler angles in Figure 4. We neglect intergrain covariance,
 356 thus the sampling error is underestimated to some extent.

357 The 90% confidence intervals of the area-weighted bootstrapped sampling distributions of $\hat{\lambda}_i$ that the estimated fabric
 358 eigenvalues $\tilde{\lambda}_i$ were assumed to be drawn from are plotted in Figure 5. For the WAIS core, the observed variability of the
 359 fabric eigenvalues over short length scales in depth seems to be primarily explained by sampling error. For the most part, it is
 360 not necessary to assume actual differences in the bulk ODF to explain these differences. The exception to this is near the bed,
 361 where there exists layers of recrystallized and non-recrystallized fabric (Fitzpatrick and others, 2014). Here, the eigenvalue
 362 differences between nearby thin sections are greater than could be expected if the thin sections were sampled from the same
 363 ODF. Indeed, in Kluskiewicz and others (2017), P-wave velocity measurements along the WAIS Divide borehole indicate low
 364 amounts of variability in the ODF over length scales of several meters in the upper 2500m of the ice core. Below this, the

Fig. 5. Estimates of the eigenvalues λ_i of the second-order orientation tensor \mathbf{A} from fabric thin sections from the WAIS Divide core. The error bars are the 90% bootstrap confidence intervals of the estimated eigenvalues $\tilde{\lambda}_i$ from the observed area-weighted thin section $\tilde{\mathbf{A}}$. Weaker fabrics near the top of the core have significant uncertainty despite larger sample-size, as is predicted by analytical estimates. The strong single-maximum fabrics seen below 3000 m have the smallest eigenvalue uncertainties. Coarse-grained, weak recrystallized fabrics near the bed exhibit the largest eigenvalue uncertainties. Thin sections at 1940 m (from Figures 3 and 4), 2905 m (Figure 1), and the multiple maximum thin sections at 3365 m and 3405 m are indicated.

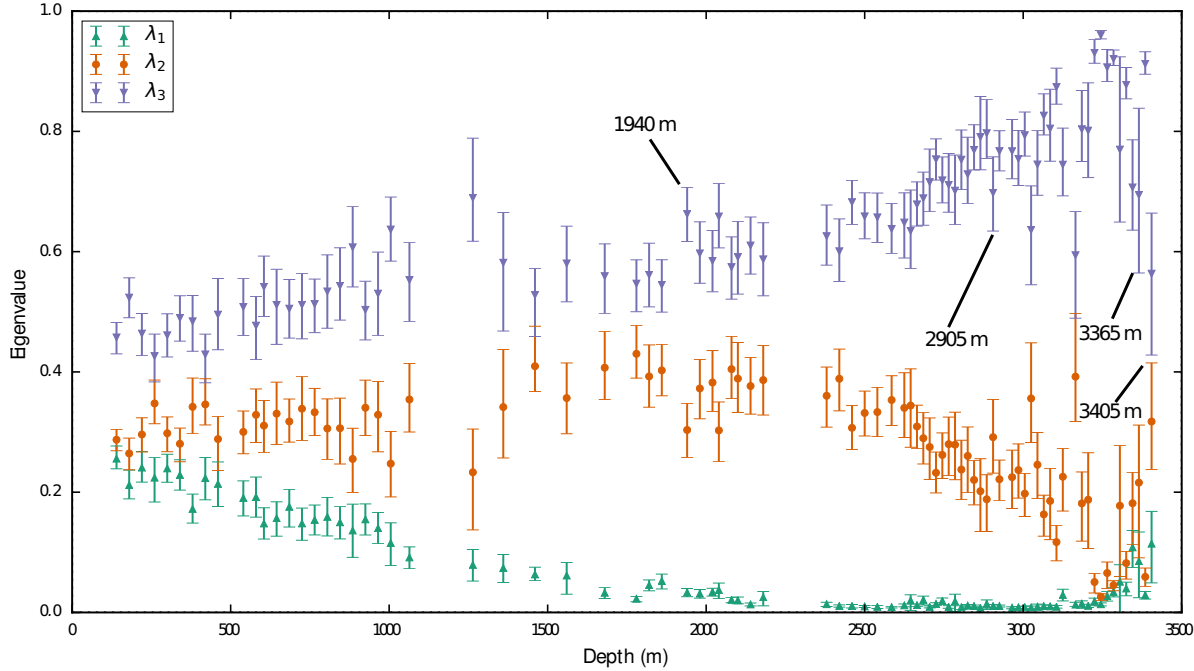
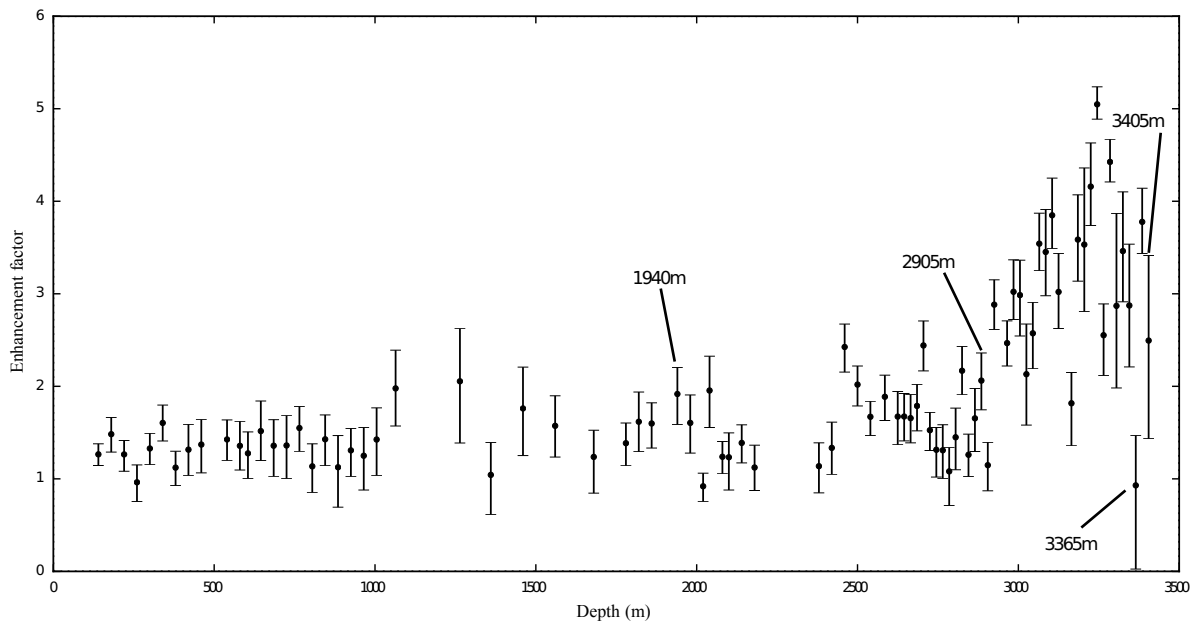


Fig. 6. Bootstrap 90% confidence intervals for enhancement factor in simple shear for the 83 WAIS thin sections. Due to the dependence on the fourth power of the average Schmid factor, the confidence intervals can be wide. Thin sections at 140m (from Figures 3, 4), 2905m (Figure 1), and the multiple maximum thin sections at 3365m and 3405m are indicated.



365 fabric inferred from P-wave velocities changes greatly over shorter length-scales. Several of the error bars are asymmetric. This
 366 typically occurs for very small or very large eigenvalues: Suppose we have a strong single maximum, with all c-axes nearly
 367 aligned, and the largest eigenvalue near unity. The eigenvalue of any resample cannot be much larger, since it cannot be greater
 368 than unity. However, if the sample has a few grains with c-axis orientations significantly differing from the maximum, they
 369 can have a proportionally greater impact on resamples of the largest eigenvalue.

370 The sampling error in this core tends to be more sensitive to fabric distribution than it is to sample size. The estimated
 371 variance of \hat{A}_{ij} in the absence of intergrain correlations, $(\mathbb{A}_{ijij} - A_{ij}A_{ij})s_n^2$ (no sum), tends to zero as fabric strength increases,
 372 towards a maximum eigenvalue of unity. In this limiting case, $\mathbb{A}_{ijij} = A_{ij}A_{ij}$ (no sum), and the eigenvalue variance is zero.
 373 Thus, sampled fabric eigenvalues and fabric eigenvectors have smaller variances for strong fabrics compared to weaker fabrics.
 374 For example, the fabric eigenvalues of the thin-section with weak fabric at 180m has similar variance to those of the strong
 375 fabric at the 3265m thin-section. This is despite the fact that the 180m thin-section has nearly three times as many sampled
 376 grains as the 3265m thin section.

377 The analytic and bootstrap estimates of sampling distributions perform similarly in weaker thin sections with larger sample
 378 sizes. However, for coarse-grained ice with small effective sample-sizes, the normal approximation of the analytic estimate is
 379 less accurate. In particular, the normal distribution has support over all real numbers. Thus, the analytic estimates of fabric
 380 eigenvalue sampling distributions may contain significant density below zero, for small eigenvalues, or greater than unity, for
 381 large ones. This is unphysical. However, the analytic estimate of variance of the sampled eigenvalues is nonetheless valid, just
 382 not the normal distribution approximation to the sampling distribution. Thus, if intergrain correlations may be discarded,
 383 bootstrap estimates of sampling error are preferred. If intergrain correlations are not negligible, however, than the bootstrap
 384 estimate of the sampling distribution underestimates the sampling error.

385 Both the analytic and bootstrap estimates of the distribution sampling error for WAIS Divide ignore intergranular covari-
 386 ances, due to the lack of connectivity data. Durand and others (2008) found that intergranular covariances are usually small
 387 unless there is active polygonization. Weikusat and others (2009) found that there was not a surplus of lower-angle boundaries
 388 between nearest-neighbor grains in comparison to random pairs in the EDML ice core. However, there is certainly active
 389 polygonization along the WAIS Divide ice core. In addition, small-scale spatial heterogeneities in the ODF may occur in the
 390 deeper core due to spatially differential dynamic recrystallization or other processes. Thus, we may underestimate the variance
 391 of sampling error for some thin sections in this core.

392 Sampling error estimates of enhancement factor

393 We now show bootstrap estimates of enhancement factor in simple shear along horizontal planes in the x -direction from the
 394 WAIS Divide ice core. In Figure 6, we used bootstrap resampling to estimate the sample distribution of the enhancement

395 factor under simple shear for each thin section in the WAIS core. Note that the 3365 m thin section does not have a vertical
 396 maximum (Fitzpatrick and others, 2014), which makes the ice harder under simple shear along horizontal planes.

397 The estimated enhancement factor errors are large for many thin sections. The enhancement factor estimated here is valid
 398 only for simple shear along horizontal planes in the x -direction. Simple shear is active mainly near the bed. However, we expect
 399 that sampling error of estimates of other rheological characteristics which depend superlinearly on resolved shear stresses of
 400 constituent grains of the polycrystal to be similarly large.

401 CONCLUSIONS

402 We compared PODFs with their log-likelihoods for different observed thin sections. This is a standard technique to fit prob-
 403 ability distributions. The Bingham distribution (4) and the Dinh-Armstrong distribution (3) perform nearly equally for the
 404 WAIS and Siple Dome ice-core thin sections. The Lliboutry distribution (1) did not fit the thin sections as well. This is chiefly
 405 because the Lliboutry distribution assumes axial symmetry. Axial symmetry, which is an assumption used by many previously
 406 proposed PODFs, is not capable of accurately approximating ODFs with three distinct fabric eigenvalues. Ice fabric in most
 407 realistic situations has three distinct eigenvalues. However, the ideal parameterized ODF may not be the same in all situations.

408 Inferring fabric from limited thin section samples is subject to sampling error. We showed analytical estimates of eigenvalue
 409 and eigenvector sampling distributions. We also examined bootstrapping of per-pixel EBSD or automatic fabric analyzer
 410 measurements of thin section data. It is necessary to use block bootstrapping to estimate uncertainties in per-pixel data, rather
 411 than ordinary bootstrapping. Ordinary bootstrapping neglects covariances between nearby pixels, which causes sampling error
 412 to be severely underestimated.

413 Sampling error estimates are sensitive to the grain size distribution. Often, thin sections are dominated by a few large grains,
 414 with many smaller ones. This results in much larger sampling uncertainties than even grain-size distributions. The estimates
 415 of sampling error distributions for the WAIS core show that fabric eigenvalues are poorly constrained for some thin sections.

416 We also showed estimates of sampling error of inferred enhancement factor in horizontal simple shear. The results indicate
 417 that sampling error in fabric may also lead to significant error in the inference of rheological characteristics of ice.

418 Sonic fabric measurements, which sample larger volumes of ice, are a promising way of overcoming sampling error (e.g., Diez
 419 and Eisen 2015, Maurel and others 2016, Kluskiewicz and others 2017). In addition, since borehole sonic velocity measurements
 420 sample several cubic meters of ice, they also reduce error due to spatial variability of the ODF when inferring fabric averaged
 421 over longer length-scales. Sonic velocity measurements based on seismic measurements (Smith and others, 2017) larger regions
 422 yet.

ACKNOWLEDGEMENTS

We thank Joan Fitzpatrick and Don Voigt for the WAIS thin-section data. We also thank Maurine Montagnat and Ilka Weikusat for helpful discussions on thin-section uncertainty. Thanks to Paul Bons, Sergio Faria, and anonymous reviewers for helpful suggestions. This work was supported by the National Science Foundation grant 1246045.

References

- Alley, R.B., 1992. Flow-law hypotheses for ice-sheet modeling, *J. Glaciol.*, **38**(129), 245–256.
- Alley, RB, AJ Gow, DA Meese, JJ Fitzpatrick, ED Waddington and JF Bolzan, 1997. Grain-scale processes, folding, and stratigraphic disturbance in the GISP2 ice core, *Journal of Geophysical Research*, **102**(C12), 26819–26.
- Azuma, N., 1994. A flow law for anisotropic ice and its application to ice sheets, *Earth and Planetary Science Letters*, **128**(3-4), 601–614.
- Azuma, N., 1995. A flow law for anisotropic polycrystalline ice under uniaxial compressive deformation, *Cold regions science and technology*, **23**(2), 137–147.
- Azuma, N. and K. Goto-Azuma, 1996. An anisotropic flow law for ice-sheet ice and its implications, *Annals of Glaciology*, **23**, 202–208.
- Azuma, N and A Higashi, 1985. Formation processes of ice fabric pattern in ice sheets, *Annals of Glaciology*, **6**(1), 130–134.
- Bingham, C., 1974. An antipodally symmetric distribution on the sphere, *The Annals of Statistics*, 1201–1225.
- Conway, H and LA Rasmussen, 2009. Recent thinning and migration of the Western Divide, central West Antarctica, *Geophysical Research Letters*, **36**(12).
- Diez, Anja and Olaf Eisen, 2015. Seismic wave propagation in anisotropic ice-Part 1: Elasticity tensor and derived quantities from ice-core properties, *The Cryosphere*, **9**(1), 367–384.
- Dinh, S. and R. Armstrong, 1984. A rheological equation of state for semiconcentrated fiber suspensions, *Journal of Rheology (1978-present)*, **28**(3), 207–227.
- Durand, G., O. Gagliardini, T. Thorsteinsson, A. Svensson, S. Kipfstuhl and D. Dahl-Jensen, 2006. Ice microstructure and fabric: an up-to-date approach for measuring textures, *Journal of Glaciology*, **52**(179), 619–630.
- Durand, G., A. Persson, D. Samyn and A. Svensson, 2008. Relation between neighbouring grains in the upper part of the NorthGRIP ice core - Implications for rotation recrystallization, *Earth and planetary science letters*, **265**(3), 666–671.
- Duval, Paul, Laurent Arnaud, Olivier Brissaud, Maureen Montagnat and Sophie de La Chapelle, 2000. Deformation and recrystallization processes of ice from polar ice sheets, *Annals of Glaciology*, **30**(1), 83–87.
- Efron, B., 1992. Bootstrap methods: another look at the jackknife, Springer.

- 452 Faria, S. H., I. Weikusat and N. Azuma, 2014. The microstructure of polar ice. Part II: State of the art, *Journal of Structural*
453 *Geology*, **61**, 21–49.
- 454 Fitzpatrick, J., D. Voigt, J. Fegyveresi, N. Stevens, M. Spencer, J. Cole-Dai, R. Alley, G. Jardine, E. Cravens, L. Wilen and
455 others, 2014. Physical properties of the WAIS Divide ice core, *Journal of Glaciology*, **60**(224), 1181.
- 456 Gagliardini, O., G. Durand and Y. Wang, 2004. Grain area as a statistical weight for polycrystal constituents, *Journal of*
457 *Glaciology*, **50**(168), 87–95.
- 458 Gagliardini, O., F. Gillet-Chaulet and M. Montagnat, 2009. A review of anisotropic polar ice models: from crystal to ice-sheet
459 flow models, *Low Temperature Science*, **68**(Supplement), 149–166.
- 460 Gagliardini, O. and J. Meyssonnier, 1999. Plane flow of an ice sheet exhibiting strain-induced anisotropy, *Advances in cold-*
461 *region thermal engineering and sciences*, Springer, 171–182.
- 462 Gillet-Chaulet, F., O. Gagliardini, J. Meyssonnier, T. Zwinger and J. Ruokolainen, 2006. Flow-induced anisotropy in polar ice
463 and related ice-sheet flow modelling, *Journal of Non-Newtonian Fluid Mechanics*, **134**(1), 33–43.
- 464 Glen, JW and MF Perutz, 1954. The growth and deformation of ice crystals, *Journal of Glaciology*, **2**(16), 397–403.
- 465 Gödert, G. and K. Hutter, 1998. Induced anisotropy in large ice shields: theory and its homogenization, *Continuum Mechanics*
466 *and Thermodynamics*, **10**(5), 293–318.
- 467 Gow, Anthony J and Debra Meese, 2007. Physical properties, crystalline textures and c-axis fabrics of the Siple Dome (Antarc-
468 *tica) ice core, Journal of Glaciology*, **53**(183), 573–584.
- 469 Hall, P., J. Horowitz and B. Jing, 1995. On blocking rules for the bootstrap with dependent data, *Biometrika*, **82**(3), 561–574.
- 470 Iliescu, D., I. Baker and H. Chang, 2004. Determining the orientations of ice crystals using electron backscatter patterns,
471 *Microscopy research and technique*, **63**(4), 183–187.
- 472 Kamb, B., 1973. Experimental recrystallization of ice under stress, Wiley Online Library.
- 473 Kennedy, J., E. Pettit and C. Di Prinzio, 2013. The evolution of crystal fabric in ice sheets and its link to climate history,
474 *Journal of Glaciology*, **59**(214), 357–373.
- 475 Kluskiewicz, D., E.D. Waddington, S. Anandakrishnan, D.E. Voigt, K. Matsuoka and M.P. McCarthy, 2017. Sonic methods
476 for measuring crystal orientation fabric in ice, and results from the West Antarctic ice sheet (WAIS) Divide, *Journal of*
477 *Glaciology*, 1–15.
- 478 Langway, C., 1959. Ice fabrics and the universal stage, Department of Defense, Department of the Army, Corps of Engineers,
479 Snow Ice and Permafrost Research Establishment.
- 480 Lile, RC, 1978. The effect of anisotropy on the creep of polycrystalline ice, *Journal of Glaciology*, **21**(85), 475–483.

- 481 Lliboutry, L., 1993. Anisotropic, transversely isotropic nonlinear viscosity of rock ice and rheological parameters inferred from
482 homogenization, *International journal of plasticity*, **9**(5), 619–632.
- 483 Mardia, K., 1975. Characterizations of directional distributions, A Modern Course on Statistical Distributions in Scientific
484 Work, Springer, 365–385.
- 485 Maurel, A., F. Lund and M. Montagnat, 2015. Propagation of elastic waves through textured polycrystals: application to ice,
486 Proc. R. Soc. A, The Royal Society, vol. 471, 20140988.
- 487 Maurel, A., J. Mercier and M. Montagnat, 2016. Critical investigation of calculation methods for the elastic velocities in
488 anisotropic ice polycrystals, *The Cryosphere*, **10**(6), 3063–3070.
- 489 Onstott, T. C., 1980. Application of the Bingham distribution function in paleomagnetic studies, *Journal of Geophysical
490 Research: Solid Earth*, **85**(B3), 1500–1510.
- 491 Pettit, E.C., T. Thorsteinsson, H.P. Jacobson and E.D. Waddington, 2007. The role of crystal fabric in flow near an ice divide,
492 *Journal of Glaciology*, **53**(181), 277–288.
- 493 Placidi, L., R. Greve, H. Seddik and S.H. Faria, 2010. Continuum-mechanical, Anisotropic Flow model for polar ice masses,
494 based on an anisotropic Flow Enhancement factor, *Continuum Mechanics and Thermodynamics*, **22**(3), 221–237.
- 495 Smith, E.C., A.F. Baird, J.M. Kendall, C. Martin, R.S. White, A.M. Brisbourne and A.M. Smith, 2017. Ice fabric in an
496 Antarctic ice stream interpreted from seismic anisotropy, *Geophysical Research Letters*, **44**(8), 3710–3718.
- 497 Staroszczyk, R. and O. Gagliardini, 1999. Two orthotropic models for strain-induced anisotropy of polar ice, *Journal of
498 Glaciology*, **45**(151), 485–494.
- 499 Svendsen, B and K Hutter, 1996. A continuum approach for modelling induced anisotropy in glaciers and ice sheets, *Annals
500 of Glaciology*, **23**(1), 262–269.
- 501 Thorsteinsson, T., 2002. Fabric development with nearest-neighbor interaction and dynamic recrystallization, *J. Geophys. Res.*,
502 **107**(2014), 10–1019.
- 503 Trefethen, L. N. and D. Bau, 1997. Numerical linear algebra, vol. 50, Siam.
- 504 Tyler, David E, 1987. Statistical analysis for the angular central Gaussian distribution on the sphere, *Biometrika*, **74**(3),
505 579–589.
- 506 Weikusat, I., S. Kipfahl, S.H. Faria, N. Azuma and A. Miyamoto, 2009. Subgrain boundaries and related microstructural
507 features in EDML (Antarctica) deep ice core, *Journal of Glaciology*, **55**(191), 461–472.
- 508 Wilen, L, 2002. Ice Fabric Characteristics: Siple Dome, A Core. Boulder, CO: National Snow and Ice Data Center.
- 509 Wilen, L. A., C. L. Diprinzio, R. B. Alley and N. Azuma, 2003. Development, principles, and applications of automated ice
510 fabric analyzers, *Microscopy research and technique*, **62**(1), 2–18.

APPENDIX A: DERIVATION OF ANALYTICAL ESTIMATES OF SAMPLING ERROR

We now derive analytical estimates for sampling error from estimating the bulk second-order orientation tensor from ice core thin sections. First, we focus on the case of per-pixel EBSD or automatic fabric analyzer measurements, which typically yield many measurements per grain. It is important to take dependence between measurements into account in this case. Samples taken from the same grain will be highly correlated, since grains are typically defined as having small misorientations (often $< 5^\circ$).

In this section, upper indices in lower-case Greek letters represent spatial locations. Upper indices in capital Greek letters represent grain indices (as opposed to indices of individual measurements). Lower indices in Roman letters are indices for tensor quantities at one location. For example, X_i^α is the i component of some tensor at spatial location α . In addition, in this section, random variables are denoted by hats (e.g. \hat{X}), and realizations of the random variables (upon measurement) are denoted by tildes (e.g. \tilde{X}).

We assume that all c-axis measurements \tilde{c}_i^α from a thin section are realizations of correlated random variables \hat{c}_i^α , where α is a spatial location in the thin section. Another realization of the thin section would produce a similar fabric. If the fabric does not differ much over shorter length scales, this could be approximated by taking another thin section from nearby ice.

While generated from the same random variables, the two thin sections would display different grain orientations and sizes.

Closer measurements are usually more correlated. Two sufficiently close measurements will usually lie in the same grain, and thus have similar orientations, under repeated realizations. This results in correlation between the two measurements. Correlation may also arise due to polygonization or small-scale strain heterogeneities.

Let \tilde{a}_{ij}^α be a realization of the ij component of the structure tensor (as a random variable) $\hat{a}_{ij}^\alpha = \hat{c}_i^\alpha \hat{c}_j^\alpha$ at spatial index α . Furthermore, let the thin-section sample estimate $\tilde{A}_{ij} = \sum_\alpha \tilde{a}_{ij}^\alpha / N$ of the component of the true second-order orientation tensor A_{ij} be a realization of $\hat{A}_{ij}^\alpha = \sum_\alpha \hat{c}_i^\alpha \hat{c}_j^\alpha / N$ (no sum), where N is the total number of measurements. We assume that each measurement is equally weighted, for simplicity of presentation. Extending these results to the case where measurements are not equally weighted is straightforward.

Suppose that we can determine the covariance between the ij component of the structure tensors at spatial locations α and β . This is given by,

$$C_{ij}^{\alpha\beta} = \text{Cov}(\hat{a}_{ij}^\alpha, \hat{a}_{ij}^\beta). \quad (\text{A1})$$

We only examine covariances between measurements of the same component of the structure tensor. We neglect the covariances between \hat{a}_{ij}^α and \hat{a}_{kl}^β where $i \neq k$ or $j \neq l$. In the reference frame defined by the eigenvectors of the true second-order orientation tensor \mathbf{A} , these covariances are zero if all \hat{a}_{ij}^α are identically distributed. They are approximately uncorrelated in the reference frame defined by the estimate $\tilde{\mathbf{A}}$. Extending the results in this section to include these covariances is straightforward. Now,

we wish to determine the variance of \hat{A}_{ij} , which the measured thin-section estimate \tilde{A}_{ij} of the true second-order orientation tensor A_{ij} is assumed to be drawn from. First, note that $\text{Var}(\hat{a}_{ij}^\alpha/N) = \text{Var}(\hat{a}_{ij}^\alpha)/N^2$. Also, the variance of a sum of random variables X_1, \dots, X_n is,

$$\text{Var}\left(\sum_i X_i\right) = \sum_{i,j} \text{Cov}(X_i, X_j) \quad (\text{A2})$$

Since $\hat{A}_{ij} = \sum_k \hat{a}_{ij}^\alpha/N$, we have,

$$\text{Var}(\hat{A}_{ij}) = \text{Var}\left(\sum_k \frac{\hat{a}_{ij}^\alpha}{N}\right) = \sum_{k,l} \frac{C_{ij}^{\alpha\beta}}{N^2} \quad (\text{A3})$$

where $C_{ij}^{\alpha\beta}$ is the covariance between the component of the structure tensor \hat{a}_{ij}^α at site α and \hat{a}_{ij}^β at site β , and N is the total number of measurements in the thin section. From the previous equation, we can see that if each structure-tensor measurement is strongly correlated with m other measurements, then the variance of \hat{A}_{ij} would be approximately m times larger than if it were uncorrelated. In a high-resolution per-pixel thin-section measurement, a single pixel can be expected to be highly correlated with many other pixels.

539 Estimation of the covariance tensor

The variance of \hat{A}_{ij} , given by (A3), depends on the covariance tensor (A1). This is typically unknown, and thus must be estimated from the thin-section data. We denote the estimate of an element of the covariance tensor from the thin-section data as $\tilde{C}_{ij}^{\alpha\beta}$. This itself can be viewed as a draw from a random variable $\hat{C}_{ij}^{\alpha\beta}$, reflecting the fact that the estimated covariance tensor estimate depends on the observed thin-section data. We now outline a method of estimating $\tilde{C}_{ij}^{\alpha\beta}$ from intergrain and intragrain sample covariances of the thin-section data.

The realization \tilde{a}_{ij}^α at spatial location α can be written as the sum

$$\tilde{a}_{ij}^\alpha = A_{ij} + \tilde{g}_{ij}^\alpha + \tilde{h}_{ij}^\alpha. \quad (\text{A4})$$

where, for an arbitrary observed grain Γ ,

$$\tilde{g}_{ij}^\alpha = \sum_{\alpha \in \Gamma} \frac{(\tilde{a}_{ij}^\alpha - A_{ij})}{n_\Gamma}, \quad (\text{A5})$$

where n_Γ is the number of measurements from observed grain Γ . The component \tilde{g}_{ij}^α can be interpreted as a component accounting for intergrain variability, and the random component \tilde{h}_{ij}^α accounts for intragrain variability. Let \hat{h}_{ij}^α be the random variable that \tilde{h}_{ij}^α was drawn from, and \hat{g}_{ij}^α be the random variable that \tilde{g}_{ij}^α was drawn from. By rearranging terms, $\tilde{h}_{ij}^\alpha = \tilde{a}_{ij}^\alpha - A_{ij} - \tilde{g}_{ij}^\alpha$. It then also follows that the sum of the intragrain component \tilde{h}_{ij}^α over all α from grain Γ is zero.

Note that we separate out \tilde{A}_{ij} , which is the expected value of \tilde{a}_{ij}^α (for all measurements α) taken over the ODF. Furthermore, we are also separating out the mean of each individual grain as well. This decomposition separates out the components of the structure tensor that vary on different length scales: global (A_{ij}), per observed grain (\tilde{g}_{ij}^α), and intragrain (\tilde{h}_{ij}^α).

We now show that the intragrain variability, \hat{h}_{ij}^α , may be ignored under some light assumptions. Intragranular misorientations within a grain occur on length scales smaller than the grain. Thus, \hat{h}_{ij}^α will typically be correlated only with other measurements that are closer than the length scales of grains. In addition, intragranular c-axis misorientations are small by definition, so covariances (as opposed to correlations) between nearby measurements will typically be small for even highly correlated nearby pairs of c-axis measurements. The critical misorientation angle distinguishing between subgrain boundary and a grain boundary is arbitrary (Faria and others, 2014). If intragranular misorientations are relatively large with respect to intergranular misorientations, such that they cannot be neglected in the variance estimate of \hat{A}_{ij} (as could be true in polygonizing strong vertical-maximum ice), then the critical angle can be redefined to be smaller. This then reduces intragranular misorientations by definition, such that $\hat{h}_{ij}^{\alpha\beta}$ may be neglected. Given these considerations, we may approximate the total covariance $C_{ij}^{\alpha\beta} \approx G_{ij}^{\alpha\beta}$, where $G_{ij}^{\alpha\beta}$ is the covariance between \hat{g}_{ij}^α and \hat{g}_{ij}^β .

We now find an estimate $\tilde{G}_{ij}^{\alpha\beta}$ of the intergranular covariance $G_{ij}^{\alpha\beta}$. Let $\hat{G}_{ij}^{\alpha\beta}$ be the random variable that $\tilde{G}_{ij}^{\alpha\beta}$ was drawn from. Note that $\tilde{g}_{ij}^\alpha = \tilde{g}_{ij}^\beta = \tilde{g}_{ij}^\Gamma$ whenever α and β lie in the same grain Γ . Now, if we assume that each \hat{g}_{ij}^α is identically distributed, and that orientations of different grains are uncorrelated, then we may approximate,

$$\tilde{G}_{ij}^{\alpha\beta} = \tilde{s}_{ij}^0 \mathbb{P}_0^{\alpha\beta}, \quad (\text{A6})$$

where $\mathbb{P}_0^{\alpha\beta} = 1$ if α and β are in the same grain, and $\mathbb{P}_0^{\alpha\beta} = 0$ otherwise. The scalar \tilde{s}_{ij}^0 is the sample variance of all g_{ij}^α . This is an unbiased estimate of the true covariance $G_{ij}^{\alpha\beta}$ if the expectation of $\hat{G}_{ij}^{\alpha\beta}$ is equal to the true value $G_{ij}^{\alpha\beta}$. This occurs if the assumptions of the estimate (identical distribution of $\hat{g}_{ij}^{\alpha\beta}$, and independence of nearest-neighbor grain orientations) are satisfied exactly.

Intergrain covariance between measurements in different grains may also be estimated from the data with simplifying assumptions. For example, in ice undergoing active polygonization, a reasonable assumption is to assume that the covariance between nearest-neighbor grains is the same value s_{ij}^1 for all pairs of measurements nearest-neighbor grains, and zero for pairs of grains which are not nearest neighbors. The nearest-neighbor covariance s_{ij}^1 may be estimated from the sample nearest-neighbor covariance \tilde{s}_{ij}^1 . In this case, we may approximate $G_{ij}^{\alpha\beta}$ as,

$$\tilde{G}_{ij}^{\alpha\beta} \approx \tilde{s}_{ij}^0 \mathbb{P}_0^{\alpha\beta} + \tilde{s}_{ij}^1 \mathbb{P}_1^{\alpha\beta}, \quad (\text{A7})$$

where $\mathbb{P}_1^{\alpha\beta} = 1$ if α and β are in neighboring grains (but not in the same grain), and $\mathbb{P}_1^{\alpha\beta} = 0$ otherwise. As with (A6), this is unbiased if the assumptions of the estimate (A7) are satisfied exactly. In a similar manner, covariances between more distant grains could also be included. For example, covariances between second-nearest neighbors could be assumed to be identical, and estimated from the sample covariance between all second-nearest neighbor pairs.

570 Note that the estimate of a single element of the covariance tensor, $(\tilde{G}_{ij}^{\alpha\beta})$ may differ greatly between realizations, for
 571 example due to different realizations having different grain sizes and orientations, and thus may differ significantly from the
 572 true covariance $G_{ij}^{\alpha\beta} \approx C_{ij}^{\alpha\beta}$. However, the effect on the variance estimate (A3) of \hat{A}_{ij} can be expected to be much smaller *as*
 573 *long as the estimate $\tilde{G}_{ij}^{\alpha\beta}$ is approximately unbiased*, and the thin section provides a reasonably representative sample from
 574 the ODF. This is because the variance estimate is formed as an average of all elements of the estimated covariance tensor.
 575 Biases may occur, for example, if nearest-neighbor covariances are neglected in polygonizing ice where such covariances are
 576 non-negligible. A larger bias may also appear if the measurements are not identically distributed, for example if the thin section
 577 is intersected by a tephra band possessing a different ODF than the surrounding ice. In such a case, it may be possible to craft
 578 a more accurate approximation of the covariance matrix, perhaps by forming separate estimates of the covariance within the
 579 tephra band and the surrounding ice. However, we do not explore such possibilities here.

Now, from (A7), $\tilde{G}_{ij}^{\alpha\beta} = \tilde{G}_{ij}^{\gamma\omega} = \tilde{K}_{ij}^{\Delta\Gamma}$ whenever α and γ lie in grain Δ , and β and ω lie in grain Γ . The same is also true
 if $\tilde{G}_{ij}^{\alpha\beta}$ is estimated without intergrain covariances (A6). Let $w^\Gamma = N^\Gamma / N$ be the proportion of observations lying in grain Γ ,
 where N^Γ is the total number of observations in grain Γ . If the number of measurements per grain is proportional to grain
 size, then this weighting coincides with area weighting of grains. We may rewrite the variance of \hat{A}_{ij} as,

$$\text{Var}(\hat{A}_{ij}) \approx w^\Delta w^\Gamma \tilde{K}_{ij}^{\Delta\Gamma}, \quad (\text{A8})$$

where the sum in Γ and Δ is taken over all grain indices in the sample. If intergrain covariances are neglected, then by (A6),
 $\tilde{K}_{ij}^{\Delta\Gamma} = \delta_{\Delta\Gamma} s_{ij}^0$, where δ_{ij} is the Kronecker delta symbol. Then, the variance may also be estimated in terms of components of
 the sample second- and fourth-order orientation tensors,

$$\begin{aligned} \text{Var}(\hat{A}_{ij}) &\approx \tilde{s}_{ij}^0 \mathbb{P}_0^{\alpha\beta} \\ &\approx \left(\langle (\hat{c}_i \hat{c}_j)^2 \rangle - \langle \hat{c}_i \hat{c}_j \rangle^2 \right) \mathbb{P}_0^{\alpha\beta} \\ &= (\mathbb{A}_{ijij} - \mathbb{A}_{ij} \mathbb{A}_{ij}) s_n^2 \\ &\approx (\tilde{\mathbb{A}}_{ijij} - \tilde{\mathbb{A}}_{ij} \tilde{\mathbb{A}}_{ij}) s_n^2. \end{aligned} \quad (\text{A9})$$

580 substantially simplifies treatment of uncertainty compared to Eq. (A3).

581 The quantity $s_n^2 = \sum_{\Delta \in \Omega} w^\Delta w^\Delta$ is the sum of squared grain weights. Note that the estimates (A8) and (A9) may be used
 582 for orientation measurements taken per-grain, as is the case with the Rigsby Stage technique, with the weightings w^Γ being
 583 done by grain area normalized to the thin-section, rather than proportional number of observations. Area weighting thus yields
 584 similar variance estimates to per-pixel measurements, if the number of per-pixel measurements in each grain is proportional
 585 to the area.

586 **Variance estimates of fabric eigenvectors and eigenvalues**

587 We now derive analytical estimates of the distribution of the eigenvectors and eigenvalues of \hat{A}_{ij} . For a large-enough sample,
 588 \tilde{A}_{ij} will have principal directions and eigenvalues close to those of A_{ij} . For a large enough number of grains, we can apply the
 589 central limit theorem to estimate the sampling distribution of \hat{A}_{ij} . As the number of sampled grains N becomes large, \hat{A}_{ij}
 590 converges in distribution to the normal distribution with mean A_{ij} and variance $\text{Var}(\hat{A}_{ij})$ (A7).

591 For simplicity, we choose to work in the reference frame defined by the three true fabric eigenvectors. In this case, A_{ij} is a
 592 diagonal matrix of the fabric eigenvalues λ_i , and the components of \hat{c}_i are uncorrelated. For a large enough number of grains,
 593 $\tilde{A}_{ij} = A_{ij} + \tilde{\epsilon}_{ij}$, where $\tilde{\epsilon}_{ij}$ is small. We can then estimate the sampled fabric eigenvalues and eigenvectors as a first-order
 594 perturbation of the original eigenvalues and eigenvectors. In this case, let A_{ij} have eigenvalues $\lambda_i = A_{ii}$ (no sum). Also, let the
 595 measured fabric sample have eigenvalues $\tilde{\lambda}_i = \lambda_i + \delta\tilde{\lambda}_i$. Then, to first order, $\delta\tilde{\lambda}_i = \tilde{\epsilon}_{ii}$ (no sum) (Trefethen and Bau, 1997).
 596 To first order, it follows that the sampling variance of corresponding random variable $\hat{\lambda}_i$ is then given by $\text{Var}(\hat{A}_{ii})$ (no sum),
 597 since $\tilde{A}_{ii} = \tilde{\lambda}_i$ (no sum).

Now that we have an estimate for the sample variance of eigenvalue estimates from thin sections, we examine sampling error of the fabric eigenvectors, or principal directions. Similarly to the eigenvalues, we use a first-order approximation of the eigenvalue perturbations (Trefethen and Bau, 1997). If we are in the reference frame defined by the true fabric eigenvectors, then the sample estimate $\tilde{\mathbf{A}}$ will be close to being diagonal, with small off-diagonal elements. The eigenvectors $\tilde{\mathbf{V}}$ of $\tilde{\mathbf{A}}$ are then,

$$\tilde{\mathbf{V}} = \begin{pmatrix} 1 & \frac{\tilde{A}_{12}}{\lambda_2 - \lambda_1} & \frac{\tilde{A}_{13}}{\lambda_3 - \lambda_1} \\ \frac{\tilde{A}_{21}}{\lambda_1 - \lambda_2} & 1 & \frac{\tilde{A}_{23}}{\lambda_3 - \lambda_2} \\ \frac{\tilde{A}_{31}}{\lambda_1 - \lambda_3} & \frac{\tilde{A}_{12}}{\lambda_2 - \lambda_3} & 1 \end{pmatrix}, \quad (\text{A10})$$

598 to first-order accuracy in \tilde{A}_{ij} . This perturbation is an infinitesimal rotation matrix, which is a first-order approximation
 599 for rotation matrices valid for small rotation angles. This defines the approximate reference frame formed by the perturbed
 600 eigenvectors. The three elements above the diagonal are the Euler angles of this infinitesimal rotation, with \tilde{V}_{23} , \tilde{V}_{13} , and \tilde{V}_{12}
 601 being realizations of the rotation angles around the z-axis, y-axis, and x-axis, respectively. As before, \hat{A}_{ij} is approximately
 602 normally distributed for a large-enough sample. The random variable \hat{V}_{12} that \tilde{V}_{12} is drawn from is then also approximately
 603 normally distributed with variance $(\lambda_2 - \lambda_1)^{-2}\text{Var}(\hat{A}_{12})$, and a mean of zero. The cases for \hat{V}_{13} and \hat{V}_{23} are similar. The true
 604 eigenvalues λ_i may be estimated from the sample eigenvalues $\tilde{\lambda}$.